Design of an Isolated Bidirectional DC–DC Converter With Built-in Filters for High Power Density

Shuntaro Inoue, *Student Member, IEEE*, Masanori Ishigaki, *Member, IEEE*, Atsuhiro Takahashi, and Takahide Sugiyama, *Member, IEEE*

***Abstract*—This article aims to realize an isolated dc–dc converter with high power density, high power efficiency, and low noise performance. Although a dual-active-half-bridge (DAHB) converter can achieve high efficiency, it requires input and output low-pass filters to suppress the operational ripple current and switching noise. Owing to the volume of the filters, a DAHB converter cannot be implemented with high power density. This article presents a design theory for a novel isolated bidirectional dc–dc converter with built-in filters. The proposed converter is derived from a DAHB converter and can eliminate the input and output filters via split windings and tank capacitors; the principle of elimination is based on *LC* low-pass filter function and zero-ripple-current operation. As the number of transistors, capacitors, and magnetic cores of the proposed converter are equal to those of the DAHB converter, the application of the proposed converter allows volume reduction by eliminating the filter components at the input and output ports. Theoretical equations are derived to design a power flow control function and a filter function simultaneously. Finally, prototypes of a DAHB converter and the proposed converter are constructed for comparison. The results demonstrate that the input port noise of the proposed prototype is lower than that of the DAHB prototype by 10 dB (peak) over 1 MHz, and the proposed approach can achieve a significant improvement in efficiency.**

***Index Terms*—Built-in filter, Ćuk converter, dual-active-bridge converter, integrated magnetic component, split windings, zero-voltage switching (ZVS).**

I. Introduction

In RECENT times, the density of power sources such as NiH and Li-ion batteries has evidently increased [1], [2]. Consequently, electric automotive systems are rapidly emerging [3], [4]. For example, electric propulsion systems [5]–[7], isolated dc–dc converters for 12-V subsystems [8]–[10], and ac–dc converters for charging systems [11]–[14] have been introduced in automotive systems. A converter is required to connect the different voltage lines in a system. Hence, the number of converters in automotive systems is increasing. Moreover, the power rating per converter is also increasing with the required power of each electric component. Consequently, the system noise, size, and heat consumption have also increased considerably over the years. Therefore, this study aims to develop a high-power-density isolated dc–dc converter with high efficiency and low noise performance.

Although several investigations have been conducted on achieving high power density, low noise, and high efficiency for isolated dc–dc converters, a definitive converter has not yet been proposed. A dual-active-half-bridge (DAHB) converter is a half-bridge-type dual-active-bridge converter that is well known as an isolated dc–dc converter for achieving high efficiency. It has a symmetric structure with phase-shift control, and it can control the isolated bidirectional power flow and zero-voltage switching (ZVS) operations for all power switches [15]–[17]. Although the DAHB converter can achieve high efficiency, it requires low-pass filters at the input and output ports to reduce current ripple and harmonics. Thus, the overall size of the converter is increased by the presence of these filters. For example, the CISPR-25 standard defines strict limits for electromagnetic interference performance for converters in automotive systems [18].

To achieve high power density, low noise, and high efficiency simultaneously, several topologies have been proposed, which attempted to reduce or eliminate the filter components, such as interleaved converter [19]–[29], multilevel converter [30]–[32], symmetrical push–pull converter [33]–[35], and isolated Ćuk converter [36]–[38]. Both the interleaved and multilevel converters can reduce the ac components of the output current at the expense of increasing the circuit complexity; however, the input and output currents still have ripple components. Although the symmetrical push–pull converter can achieve zero-ripple input current, the voltage waveforms exhibit ringing during the dead-time period owing to the leakage inductance energy; hence, a filter component is still required at the input port of this converter. An isolated Ćuk converter with an integrated magnetic component can achieve zero-ripple input and output currents as well as control bidirectional power flows. However, it has to be operated in the hard-switching condition, which causes a reduction in efficiency. Moreover, it is difficult to implement unbalanced leakage inductances in an integrated magnetic component.

A novel isolated bidirectional dc–dc converter with built-in filters has been proposed in [39]. A simple circuit implementation and zero-ripple input and output currents can be achieved

Manuscript received September 3, 2019; revised January 15, 2020 and April 28, 2020; accepted June 2, 2020. Date of publication June 18, 2020; date of current version September 4, 2020. This paper was presented in part at the 2019 IEEE Applied Power Electronics Conference and Exposition, Anaheim, CA, USA, Mar. 17–21, 2019. Recommended for publication by Associate Editor D. Xu. *(Corresponding author: Shuntaro Inoue.)*

The authors are with the Department of System and Electronics Engineering II, Toyota Central R&D Labs., Inc., Nagakute 480-1192, Japan (e-mail: shuntaro0628@gmail.com; masanori.ishigaki@toyota.com; a-takahashi@mosk.tytlabs.co.jp; t-sugiyama@mosk.tytlabs.co.jp).

Color versions of one or more of the figures in this article are available online at https://ieeexplore.ieee.org.

Digital Object Identifier 10.1109/TPEL.2020.3003618

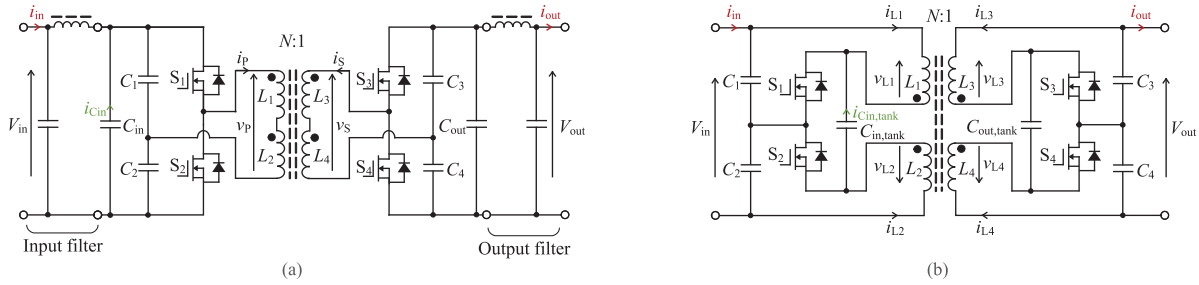

Fig. 1. Circuit diagrams of (a) the DAHB converter with input and output LC low-pass filters and (b) the proposed converter with built-in filters.

in ZVS operation using the proposed converter. Furthermore, the proposed converter has the potential to achieve compact and high-efficiency dc–dc conversion by eliminating the input and output filters owing to the zero-ripple operation and LC low-pass filter function.

This article presents a design theory for the proposed converter using the simulation results of the leakage inductance and the loss of the magnetic components of the proposed converter obtained via a three-dimensional model. Furthermore, experimental results with regard to the noise and efficiency of the proposed converter, obtained from prototypes, are also presented. Moreover, as an extension of the proposed topology, a full-bridge-type dc–dc converter with built-in filters is elucidated in the final part of this article.

II. Proposed Converter With Built-in Filters

Fig. 1 shows the circuit diagrams of a conventional DAHB converter with filters and the proposed converter. Fig. 1(a) shows the DAHB converter. To clarify the difference between the DAHB converter and the proposed converter, the DAHB converter is represented using split windings. Fig. 1(b) shows the proposed converter. The numbers of transistors and capacitors used in the proposed converter and the required breakdown voltages of these transistors and capacitors are the same as those of the DAHB converter.

The proposed converter is based on two principles for eliminating the input and output filter components. The first principle concerns the LC low-pass filter function. The proposed converter can add an LC low-pass filter function using the leakage inductance between the split windings. Fig. 2 shows the leakage magnetic fields of the proposed converter for the operational current and harmonic switching current flows. In Fig. 2, the leakage magnetic coefficient between L_{m} and L_{n} is represented as $k_{\mathrm{m,n}}$ (m, n: natural number) and defined using k_{PP}, k_{SS}, and k_{PS} as follows:

$$k_{12} \equiv k_{\mathrm{PP}} \tag{1}$$

$$k_{34} \equiv k_{\mathrm{SS}} \tag{2}$$

$$k_{13} = k_{14} = k_{23} = k_{24} \equiv k_{\mathrm{PS}}. \tag{3}$$

Fig. 2(a) shows the leakage magnetic field induced by the operational currents of the dc–dc converter function. The solid line shows an ac component of the operational current. The dot line shows a magnetic field produced by the ac component of the operational current. Because the magnetic field is generated between the primary windings and the secondary windings, the leakage magnetic inductance generated by the magnetic field can be used for the dc–dc function as with the conventional DAHB converter. The leakage inductance can be designed using the coupling coefficient k_{PS} between the primary-side and secondary-side windings. Fig. 2(b) shows the leakage magnetic field induced by the switching noise. The solid line shows the switching noise and current. The dot line shows the magnetic field produced by the switching noise and current. The magnetic field is induced in an area between two primary windings. The leakage magnetic inductance generated by this magnetic field can be used for the inductances of the LC low-pass filter function. The leakage inductance can be designed using the coefficient k_{PP} between the two primary windings. Moreover, the series-connected capacitors, C_1 and C_2, can be used as the capacitors of the LC low-pass function.

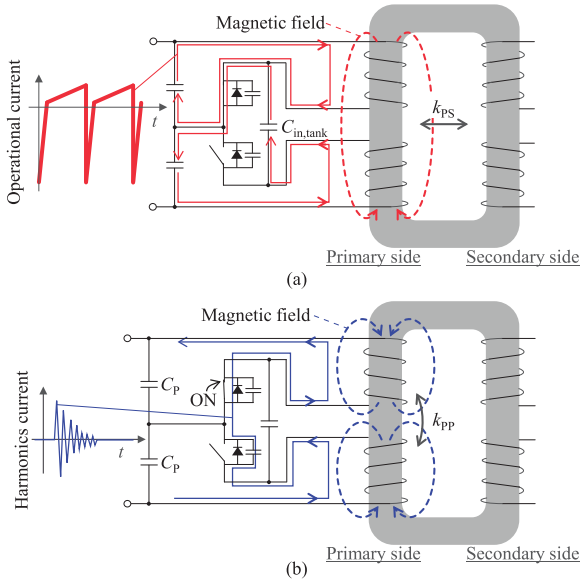

Fig. 2. Magnetic leakage fields against (a) operational current and (b) harmonics current caused by switching.

The second principle is the zero-current-ripple operation. Fig. 3 shows the theoretical waveforms of the DAHB converter

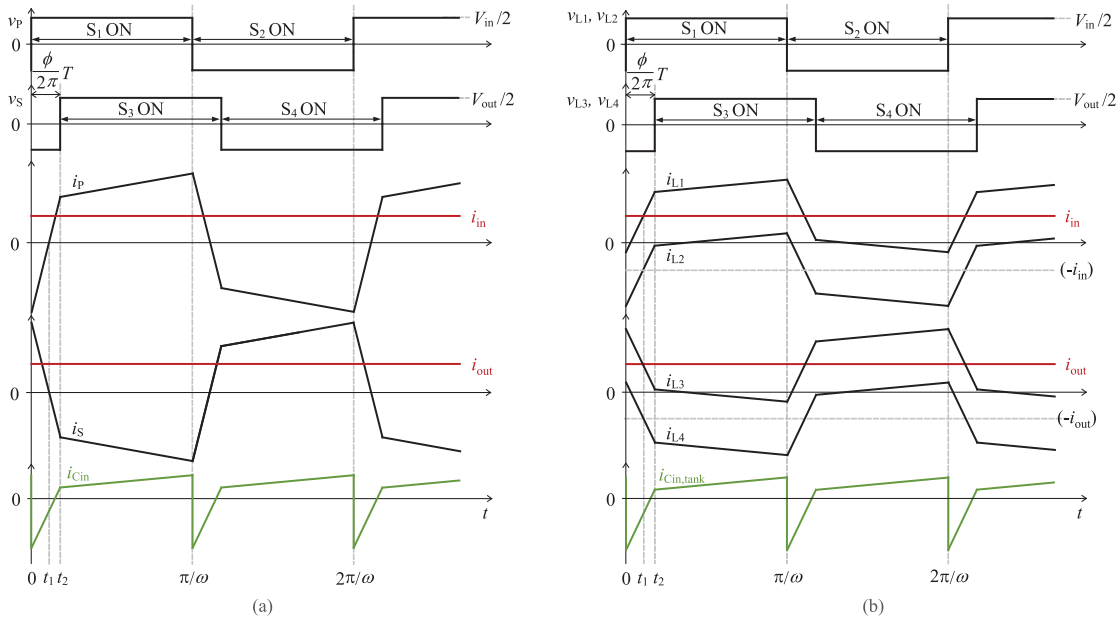

Fig. 3. Ideal waveforms of (a) the DAHB converter with input and output LC low-pass filters and (b) the proposed converter with built-in filters.

and the proposed converter. To derive the ideal waveforms, the following restrictions are assumed:

1) all the transistors are ideal switches;
2) the dead time is ignored;
3) the parasitic components are ignored.

Fig. 3(a) depicts the theoretical waveforms of the DAHB converter. A ripple current $i_{\rm Cin}$ flows into the input port capacitor $C_{\rm in}$. The power flow can be controlled by the phase difference ϕ between the primary-side transistors and the secondary-side transistors. Fig. 3(b) depicts the theoretical waveforms of the proposed converter. The control strategy for the bidirectional power flow is the same as that of the DAHB converter. The proposed converter has dc power flow from input power source to the tank capacitor $C_{\rm in,tank}$, and from the tank capacitor $C_{\rm out,tank}$ to output load, respectively. Thus, the currents in winding $i_{\rm L1}$, $i_{\rm L2}$, $i_{\rm L3}$, and $i_{\rm L4}$ have dc components. The input current $i_{\rm in}$ and output current $i_{\rm out}$ are zero-ripple currents, as the positions of the input and output capacitors for mitigation of the current ripple are moved to the insides of the converter, as indicated by tank capacitors $C_{\rm in,tank}$ and $C_{\rm out,tank}$, respectively.

As the positive half-cycle is symmetrical to the negative half-cycle in the proposed topology, the description of the proposed circuit operation will focus only on the positive half-cycle. Under steady-state operation, the proposed converter has three operation stages within the half-cycle as follows.

Subinterval 1 $(0 \le t < t_1)$*:* Transistors $\rm S_1$ and $\rm S_4$ are in the ON-state, and the primary currents $i_{\rm L1}$ and $i_{\rm L2}$ increase. Magnetic energy is charged in the leakage inductance $L_{\rm eq}$ between the primary-side windings (L_1, L_2) and the secondary-side windings (L_3, L_4).

Subinterval 2 $(t_1 \le t < t_2)$*:* The primary currents $i_{\rm L1}$ and $i_{\rm L2}$ exceed the input port current $i_{\rm in}$ and negative value of input port current $-i_{\rm in}$, respectively. The secondary currents $i_{\rm L3}$ and $i_{\rm L4}$ are below the output port current $i_{\rm out}$ and its negative value $-i_{\rm out}$, respectively. As the currents through the transistors on the primary and secondary sides are represented as $i_{\rm L1} + i_{\rm L2}$ and $i_{\rm L3} + i_{\rm L4}$, respectively, the directions of the currents in the transistors also change from this subinterval.

Subinterval 3 $(t_2 \le t < \pi/\omega)$*:* Transistors $\rm S_1$ and $\rm S_3$ are in the ON-state. According to the constant current function of the charged magnetic energy in the leakage inductance $L_{\rm eq}$, the currents in the windings flow from $V_{\rm in}$ to $V_{\rm out}$, and the electric power is delivered from the input port to the output port.

As shown in Fig. 3(b), the proposed converter can achieve zero-ripple operation without input and output filters. In subintervals 1 and 2, the DAHB converter charges the current from the input capacitor $C_{\rm in}$ to a leakage inductance between the primary windings and the secondary windings. The charged current causes current ripples in the input and output ports. As for the proposed converter, the charged current is supplied from a tank capacitor $C_{\rm in,tank}$. As a result, the proposed converter does not have input or output current ripples. Based on the LC low-pass filter function and the zero-current-ripple operation, the proposed converter can help eliminate the input and output filter components.

III. Analysis and Design of the Proposed Converter

Analysis and design were first considered in constructing the proposed converter.

A. Theoretical Equation of Power Flow

The theoretical equation for the delivered power against the phase difference ϕ is derived to design the proposed converter. The theoretical equation of power flow for the DAHB converter

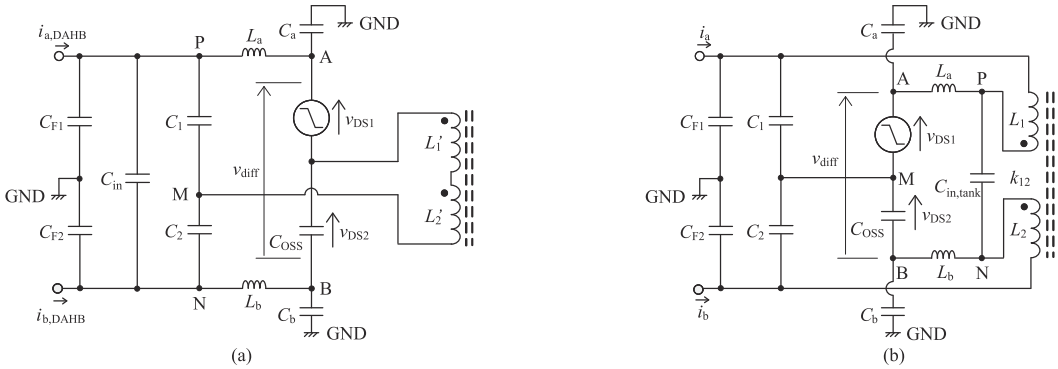

Fig. 4. Primary-side circuits with parasitic components when the upper-side transistor is turned ON. (a) DAHB converter. (b) Proposed converter.

is written as follows:

$$P_{\mathrm{out,DAHB}} = \frac{NV_{\mathrm{in}}V_{\mathrm{out}}}{4\pi\omega L_{\mathrm{eq,DAHB}}}\phi(\pi - |\phi|) \ \ (-\pi \le \phi \le \pi) \quad (4)$$

where $L_{\mathrm{eq,DAHB}}$ is the total leakage inductance of the transformer in the DAHB converter, expressed as follows:

$$L_{\mathrm{eq,DAHB}} = 2(L'_{\mathrm{P}} + k'_{\mathrm{PP}}L'_{\mathrm{P}} + N^2\,L'_{\mathrm{S}} + N^2\,k'_{\mathrm{SS}}L'_{\mathrm{S}}) - 8\,Nk'_{\mathrm{PS}}\sqrt{L'_{\mathrm{P}}L'_{\mathrm{S}}} \quad (5)$$

where L'_{P} and L'_{S} are defined as follows:

$$L'_1 = L'_2 \equiv L'_{\mathrm{P}} \quad (6)$$

$$L'_3 = L'_4 \equiv L'_{\mathrm{S}}. \quad (7)$$

Similarly, the output power P_{out} of the proposed converter can be written as follows:

$$P_{\mathrm{out}} = \frac{NV_{\mathrm{in}}V_{\mathrm{out}}}{\pi\omega L_{\mathrm{eq}}}\phi(\pi - |\phi|) \ \ (-\pi \le \phi \le \pi) \quad (8)$$

where L_{eq} is the total leakage inductance of the transformer in the proposed converter, expressed as

$$L_{\mathrm{eq}} = 2(L_{\mathrm{P}} + k_{\mathrm{PP}}L_{\mathrm{P}} + N^2L_{\mathrm{S}} + N^2k_{\mathrm{SS}}L_{\mathrm{SS}}) - 8\,Nk_{\mathrm{PS}}\sqrt{L_{\mathrm{P}}L_{\mathrm{S}}} \quad (9)$$

where L_{P} and L_{S} are defined as follows:

$$L_1 = L_2 \equiv L_{\mathrm{P}} \quad (10)$$

$$L_3 = L_4 \equiv L_{\mathrm{S}}. \quad (11)$$

Equations (5) and (9) demonstrate that the proposed converter has the same leakage inductance as the DAHB converter. Meanwhile, (4) and (8) indicate that the proposed converter can control a power range four times larger than that of the DAHB with the same configuration for the transformer windings and the core.

B. LC Low-Pass Filter Function for Switching Noise

Fig. 4 presents the primary-side circuit diagrams of the DAHB and proposed converters with parasitic components [40]–[42], when the upper-side transistor is switched ON from the dead time interval. C_{a} and C_{b} are the total capacitances between the power lines, and the heat sinks are connected to the casing ground via insulator. When the upper-side transistor is switched ON, C_{a} has a sufficiently larger capacitance value than C_{b}. When the lower-side transistor is switched ON, C_{b} has a sufficiently larger capacitance value than C_{a} [42]. L_{a} and L_{b} are the parasitic inductances of the power lines. The capacitance between the drain and source of the lower-side transistor is represented as C_{OSS}. Fig. 4(a) depicts the circuit diagram of the DAHB converter. When the upper-side transistor of the DAHB converter is turned ON, the drain–source voltage v_{DS1} of S_1 changes from V_{in} to 0, and it can be expressed as follows:

$$v_{\mathrm{DS1}}(t) = -k_{\mathrm{v}}t\,(t > 0) \quad (12)$$

where k_{v} is the amount of change in the drain–source voltage defined by the physical characteristics of the transistor and the gate resistance. As v_{DS1} changes like a ramp function, v_{DS2} vibrates, and the voltage $v_{\mathrm{diff}}(= v_{\mathrm{DS1}} + v_{\mathrm{DS2}})$ becomes a noise source. Fig. 4(b) shows the circuit diagram of the proposed converter. The noise source construction is the same as that in the DAHB converter.

Fig. 5 illustrates the differential-mode equivalent circuits of the DAHB converter [42] and the proposed converter. The parasitic components L_{a}, L_{b}, C_{a}, and C_{b} are approximated to zero. The input port capacitor C_{in}, tank capacitor $C_{\mathrm{in,tank}}$, and common-mode-noise capacitors C_{F1} and C_{F2} are avoided because their influences on the differential-mode current $(i_{\mathrm{a}} - i_{\mathrm{b}})/2$ are small. Fig. 5(a) shows the equivalent circuit of the DAHB converter for the differential mode. The noise source is directly connected to the input port. Fig. 5(b) displays the equivalent circuit of the proposed converter for the differential mode. In contrast to the DAHB converter, the proposed converter inserts leakage inductances $(1 - k_{12})L_1 + (1 - k_{12})L_2$ between the noise source voltage v_{diff} and the port voltage $v_{\mathrm{diff,out}}$. Therefore, the proposed converter can filter the differential-mode current generated from the noise source voltage v_{diff} by using the LC low-pass filter comprising $(1 - k_{12})L_1$, $(1 - k_{12})L_2$, C_1, and C_2.

Fig. 6 presents the common-mode equivalent circuits of the DAHB [42] and proposed converters over an operational switching frequency. The common-mode equivalent circuits are driven by assuming that the impedances of C_{in}, $C_{\mathrm{in,tank}}$, C_1, and C_2 are regarded as short circuits because these components are

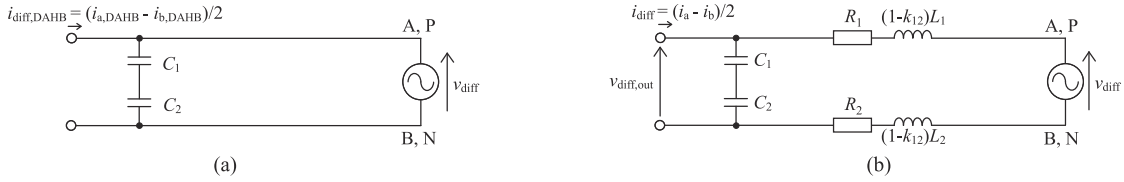

Fig. 5. Equivalent circuit for the differential-mode current of each topology. (a) DAHB converter. (b) Proposed converter.

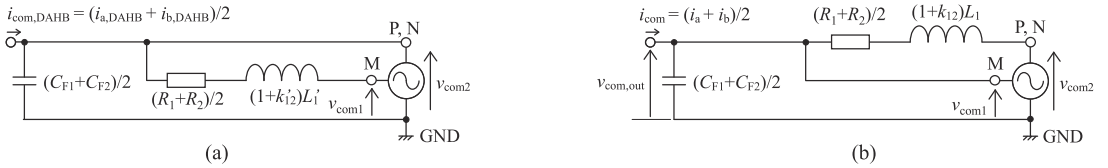

Fig. 6. Equivalent circuit for the common-mode current of each topology. (a) DAHB converter. (b) Proposed converter.

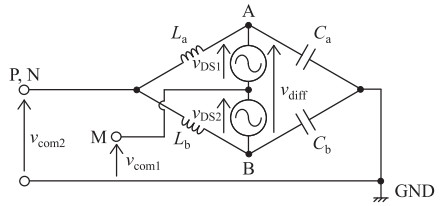

Fig. 7. Conversion from the differential-mode-noise voltage source $v_{\rm diff}$ to the common-mode-noise voltage sources $v_{\rm com1}$ and $v_{\rm com2}$.

sufficiently small compared to $C_{\rm a}$, $C_{\rm b}$, $C_{\rm F1}$, and $C_{\rm F2}$ over the operational switching frequency.

Fig. 7 presents a bridge circuit comprising $L_{\rm a}$, $L_{\rm b}$, $C_{\rm a}$, and $C_{\rm b}$. The bridge circuit has common-mode-noise voltage sources $v_{\rm com1}$ and $v_{\rm com2}$. $v_{\rm com1}$ is caused by the series-connected voltage vibration of $v_{\rm DS1}$ and $C_{\rm a}$ or $v_{\rm DS2}$ and $C_{\rm b}$. Hence, $v_{\rm com1}$ increases as the values of $C_{\rm a}$ and $C_{\rm b}$ increase. $v_{\rm com2}$ can be regarded as the output voltage of the bridge circuit, and $v_{\rm diff}$ is regarded as the input voltage. Therefore, $v_{\rm com2}$ is considerably affected by the imbalance of $L_{\rm a}$, $L_{\rm b}$, $C_{\rm a}$, and $C_{\rm b}$.

Fig. 6(a) shows an equivalent circuit of the DAHB converter for the common mode. A self-inductance $(1+k_{12})L'_1$ is connected between $v_{\rm com1}$ and the input port. Fig. 6(b) depicts an equivalent circuit of the proposed converter for the common mode. Compared with the DAHB converter, the proposed converter has a self-inductance $(1+k_{12})L_1$ between $v_{\rm com2}$ and $v_{\rm com,out}$, at the expense of removing the inductance between $v_{\rm com1}$ and $v_{\rm com,out}$. Accordingly, if unbalancedness of the bridge impedance is high, the common-mode noise $v_{\rm com,out}$ is smaller than that of the DAHB converter, because $v_{\rm com2}$ is suppressed by the inserted inductance $(1+k_{12})L_1$. The proposed converter is affected by a common-mode noise greater than that in the DAHB converter, if the bridge circuit composed of parasitic components $L_{\rm a}$, $L_{\rm b}$, $C_{\rm a}$, and $C_{\rm b}$ is well balanced, and $v_{\rm com2}$ is smaller than $v_{\rm com1}$. As the capacitance values of $C_{\rm a}$ and $C_{\rm b}$ are significantly different, as described above, the bridge circuit is well balanced in very few cases [42].

C. Theoretical Equations of Filter Functions

The theoretical equations of the filter functions in the proposed converter for each current mode are written as follows.

1) Differential Mode: The transfer function $v_{\rm diff,out}/v_{\rm diff}$ of the differential filter function is written as follows:

$$\frac{v_{\rm diff,out}}{v_{\rm diff}} = \frac{\frac{1}{L_{\rm diff}C_{\rm diff}}}{s^2 + \frac{R_{\rm diff}}{L_{\rm diff}}s + \frac{1}{L_{\rm diff}C_{\rm diff}}} \tag{13}$$

where $L_{\rm diff}$ and $C_{\rm diff}$ are defined as

$$L_{\rm diff} = (1-k_{12})L_1 + (1-k_{12})L_2 \tag{14}$$

$$C_{\rm diff} = \frac{C_1C_2}{C_1+C_2}. \tag{15}$$

$R_{\rm diff}$ is defined as follows when the series of resistances L_1 and L_2 are assumed as R_1 and R_2, respectively:

$$R_{\rm diff} = R_1 + R_2. \tag{16}$$

The cutoff frequency of the differential-mode filter function is obtained as follows when the resistance of $R_{\rm diff}$ is considerably smaller than the absolute values of the impedances of $L_{\rm diff}$ and $C_{\rm diff}$:

$$f_{\rm diff} = \frac{1}{2\pi\sqrt{L_{\rm diff}C_{\rm diff}}}. \tag{17}$$

2) Common Mode: The transfer function $v_{\rm com,out}/v_{\rm com2}$ is written as follows:

$$\frac{v_{\rm com,out}}{v_{\rm com2}} = \frac{\frac{1}{L_{\rm com}C_{\rm com}}}{s^2 + \frac{R_{\rm com}}{L_{\rm com}}s + \frac{1}{L_{\rm com}C_{\rm com}}} \tag{18}$$

where $L_{\rm com}$, $C_{\rm com}$, and $R_{\rm com}$ are

$$L_{\rm com} = (1+k_{\rm PP})L_{\rm P} \tag{19}$$

$$C_{\rm com} = \frac{C_{\rm F1}+C_{\rm F2}}{2} \tag{20}$$

$$R_{\rm com} = \frac{R_1+R_2}{2}. \tag{21}$$

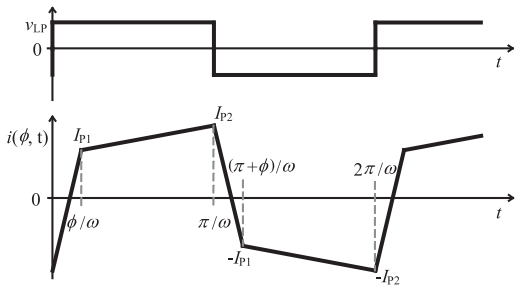

Fig. 8. Example of primary voltage and current waveforms.

The cutoff frequency of the common-mode filter function is derived as follows when the resistance $R_{\rm com}$ is considerably smaller than the absolute values of the impedances of $L_{\rm com}$ and $C_{\rm com}$:

$$f_{\rm com} = \frac{1}{2\pi\sqrt{L_{\rm com}C_{\rm com}}}. \tag{22}$$

D. ZVS Analysis

In this section, ZVS region when transistors are turned ON is investigated. Although the proposed converter has dc bias in the transformer windings, the sum of the currents in the transistors on the same side has no dc bias because the transistor currents are the sum of the two currents in the windings on the same side. Hence, for analysis of the ZVS region, the input current $i(\phi, t)$ is defined as $i(\phi, t) = i_{\rm L1}(\phi, t) + i_{\rm L2}(\phi, t)$. In each subinterval, the input current $i(\phi, t)$ is depicted as shown in Fig. 8, and it is written as follows:

$$i(\phi,t) = -I_{\rm P2} + \frac{V_{\rm in}+NV_{\rm out}}{L_{\rm eq}}t, \left(0 \le t < \frac{\phi}{\omega}\right) \tag{23}$$

$$i(\phi,t) = I_{\rm P1} + \frac{V_{\rm in}-NV_{\rm out}}{L_{\rm eq}}t, \left(\frac{\phi}{\omega} \le t < \frac{\pi}{\omega}\right) \tag{24}$$

$$i(\phi,t) = I_{\rm P2} - \frac{V_{\rm in}+NV_{\rm out}}{L_{\rm eq}}t, \left(\frac{\pi}{\omega} \le t < \frac{\pi+\phi}{\omega}\right) \tag{25}$$

$$i(\phi,t) = -I_{\rm P1} - \frac{V_{\rm in}-NV_{\rm out}}{L_{\rm eq}}t, \left(\frac{\pi+\phi}{\omega} \le t < \frac{2\pi}{\omega}\right) \tag{26}$$

where $I_{\rm P1}$ and $I_{\rm P2}$ are defined as the currents at $t = \phi/\omega$ and $t = \pi/\omega$, respectively.

If $I_{\rm P1}$ is positive, the output-side transistors $\rm S_3$ and $\rm S_4$ achieve ZVS. Similarly, if $I_{\rm P2}$ is positive, the input-side transistors $\rm S_1$ and $\rm S_2$ achieve ZVS. Hence, the ZVS requirements can be written as follows:

$$I_{\rm P1} = \frac{(\phi-\pi)V_{\rm in} + 2\phi NV_{\rm out}}{2\omega L_{\rm eq}} > 0 \tag{27}$$

$$I_{\rm P2} = \frac{(\pi-\phi)V_{\rm in} - 2(\pi-2\phi)NV_{\rm out}}{2\omega L_{\rm eq}} > 0. \tag{28}$$

By rearranging (27) and (28), the ZVS boundaries are represented as follows:

$$\phi = \frac{\pi}{2}\left(1 - \frac{NV_{\rm out}}{V_{\rm in}}\right) \tag{29}$$

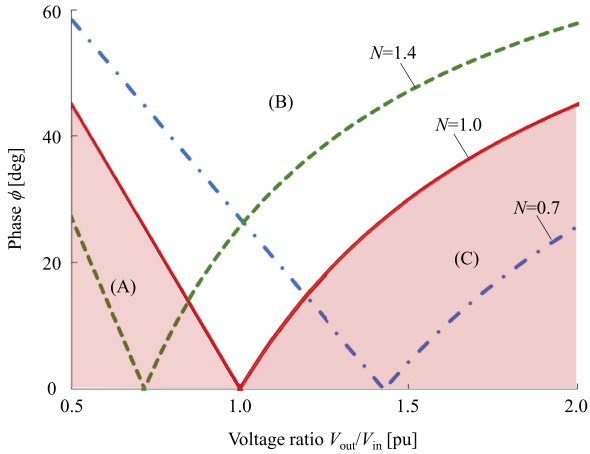

Fig. 9. ZVS region of the proposed converter.

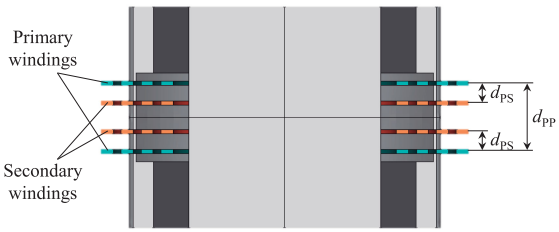

Fig. 10. Cross section of three-dimensional magnetic component model for FEM simulation.

$$\phi = \frac{\pi}{2}\left(1 - \frac{V_{\rm in}}{NV_{\rm out}}\right). \tag{30}$$

When $N = 1.0$ and $V_{\rm out}/V_{\rm in} < 1.0$, the ZVS boundary is expressed by (29), and when $N = 1.0$ and $V_{\rm out}/V_{\rm in} \ge 1.0$, the ZVS boundary is expressed by (30).

Fig. 9 shows the ZVS regions when the winding ratio N is changed in three patterns. As the ZVS boundary equation is changed according to the voltage ratio $V_{\rm out}/V_{\rm in}$, the regions are divided into three areas as follows.

A) The input-side transistors $\rm S_1$ and $\rm S_2$ are operated in the hard-switching mode, and the output-side transistors $\rm S_3$ and $\rm S_4$ are operated in the ZVS mode.
B) All the transistors can achieve ZVS.
C) The input-side transistors $\rm S_1$ and $\rm S_2$ are operated in the ZVS mode, and the output-side transistors $\rm S_3$ and $\rm S_4$ are operated in the hard-switching mode.

The result of the ZVS region analysis shows that the ideal ZVS region of the proposed converter shown in Fig. 9 becomes exactly the same as that of the DAHB converter [15]–[17].

E. Design Independence Between $k_{\rm PP}$ and $k_{\rm PS}$

The proposed converter uses two leakage inductances for the dc–dc function and LC low-pass filter function. This section discusses the design independence between the two leakage inductances. Fig. 10 shows a cross section of the three-dimensional magnetic component model developed for the finite-element

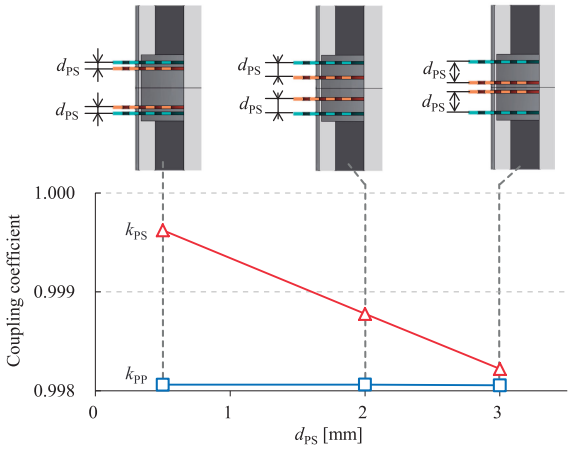

Fig. 11. Simulation result of the relationship between k_{PS}, k_{PP}, and d_{PS} when d_{PP} is fixed at 8.0 mm.

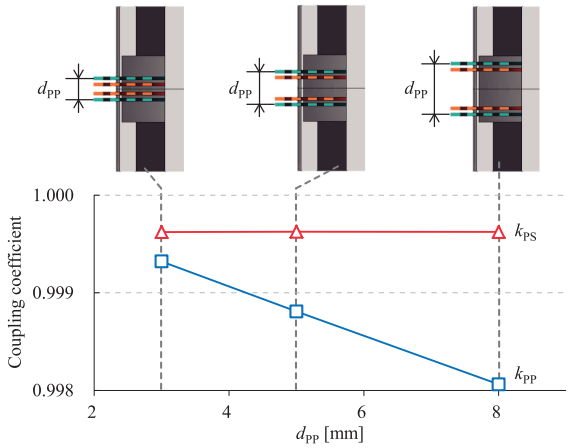

Fig. 12. Simulation result of the relationship between k_{PS}, k_{PP}, and d_{PP} when d_{PS} is fixed at 0.5 mm.

method (FEM) simulation. The parameters of the core shape are set as those of PC95PQ60/40 (TDK). The turn number of each of the windings is set to 4. The windings located outside are primary windings, whereas the windings located at the center are secondary windings. k_{PS} is calculated as the mean value of k_{13}, k_{14}, k_{23}, and k_{24}.

Fig. 11 shows a simulation result of the relationship between k_{PS}, k_{PP}, and d_{PS} when d_{PP} is fixed at 8.0 mm. In this situation, only k_{PS} is decreased linearly by increasing the distance d_{PS}.

Fig. 12 shows a simulation result of the relationship between k_{PS}, k_{PP}, and d_{PP} when d_{PS} is fixed at 0.5 mm. In this situation, only k_{PP} can be decreased linearly by increasing the distance d_{PP}.

The aforementioned results indicate that k_{PS} and k_{PP} can be designed with d_{PS} and d_{PP}, independently. Hence, by varying the distance d_{PS} between the primary windings and the secondary windings, the magnetic coefficient k_{PS} can be varied to design the dc–dc function. By changing the distance d_{PP} between two primary windings, the magnetic coefficient k_{PP} can be varied to design the LC low-pass filter function.

TABLE I
SIMULATION PARAMETERS OF THE DAHB CONVERTER AND THE PROPOSED CONVERTER INCLUDING THE PARASITIC COMPONENTS

Description	Property	
Switching frequency	f_{sw}	200 kHz
Output power	P_{out}	500 W
Input and output DC voltage	V_{in}, V_{out}	48 V, 48 V
DC capacitor	C_1, C_2 C_3, C_4	150 μF
DC capacitor	C_{in}, C_{out}	90 μF
DC capacitor	$C_{in,tank}$, $C_{out,tank}$	90 μF
Self-inductance of primary side	L_1', L_2' L_1, L_2	80 μH, 80 μH 320 μH, 320 μH
Self-inductance of secondary side	L_3', L_4' L_3, L_4	80 μH, 80 μH 320 μH, 320 μH
Coupling coefficient	k_{PP}	0.997
Coupling coefficient	k_{PS}	0.998
Drain-source capacitor of a transistor	C_{OSS}	1000 pF
Parasitic capacitors	C_a, C_b	150 pF, 1pF
Capacitors for common-mode filter	C_{F1}, C_{F2}	2 nF
Parasitic inductances	L_a, L_b	50 nH
Rise time of transistors	T_{rise}	9.9 ns
Fall time of transistors	T_{fall}	3.9 ns

F. Theoretical Equations of Maximum Magnetic Density

The magnetic flux density of the DAHB converter, $B_{0-P,DAHB}$, and that of the proposed converter, B_{0-P}, are written as follows:

$$B_{0-P,DAHB} = \frac{\pi V_{in}}{8\omega(N_{L1'} + N_{L2'})A} \tag{31}$$

$$B_{0-P} = \frac{\pi V_{in}}{4\omega(N_{L1} + N_{L2})A} \tag{32}$$

where $N_{L1'}$, $N_{L2'}$, N_{L1}, and N_{L2} are the numbers of turns of L_1', L_2', L_1, and L_2, respectively, and A is the effective cross section of the magnetic core. As the directions of the split windings of the proposed converter are inverted between L_1 and L_2, the dc magnetic fluxes caused by the dc are canceled. Therefore, the core gap is not required, and the design method for the magnetic core of the DAHB converter can be applied to the proposed converter.

G. Simulation Analysis of Noise Characteristics

The validity of the differential-mode and common-mode filter functions is discussed using a circuit simulator (LTspice). Table I summarizes the simulation parameters, including the parasitic components. Based on [42], C_a and C_b are set to 150 and 1 pF, respectively. To convert the measured current value to the power value, the conversion factor from current to voltage is set as 1, and the input impedance is set as 50 Ω.

Fig. 13 shows the simulation results of the differential-mode noise at 500 W. $i_{diff,DAHB}$ and i_{diff} are the differential-mode currents defined as follows:

$$i_{diff,DAHB} = (i_{a,DAHB} - i_{b,DAHB})/2 \tag{33}$$

$$i_{diff} = (i_a - i_b)/2. \tag{34}$$

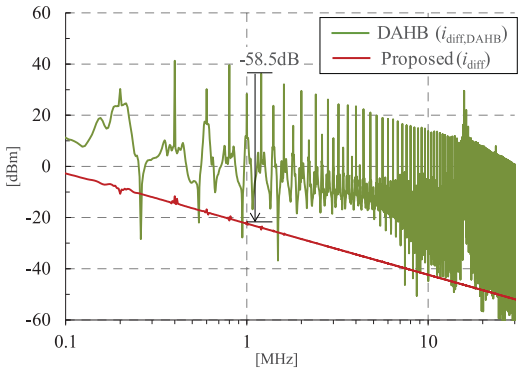

Fig. 13. Simulation result of differential-mode noise spectrum.

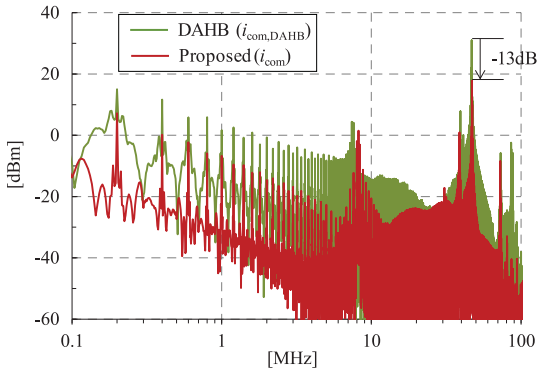

Fig. 14. Simulation result of common-mode noise spectrum.

Since the proposed converter has the LC low-pass filter function and the zero-current-ripple feature, differential noise of the proposed converter is almost zero in the ideal situation. On the frequency band over 1 MHz, the peak amplitude of the differential-mode current is suppressed by 58.5 dB. If the coupling coefficient k_{12} is higher, the benefit of the noise reduction is decreased. Unbalancedness of capacitors C_1 and C_2 or L_1 and L_2 also causes the reduction in the benefit.

Fig. 14 shows the simulation results of the common-mode noise at 500 W. $i_{\mathrm{com,DAHB}}$ and i_{com} are the common-mode currents, which are defined as follows:

$$i_{\mathrm{com,DAHB}} = (i_{\mathrm{a,DAHB}} + i_{\mathrm{b,DAHB}})/2 \tag{35}$$

$$i_{\mathrm{com}} = (i_{\mathrm{a}} + i_{\mathrm{b}})/2. \tag{36}$$

At approximately 45 MHz, there are peaks of noises that are caused by the vibrations of the drain–source voltage of transistors, defined by T_{rise} and T_{fall}. The simulation result demonstrates that, compared with the DAHB converter, the proposed converter can suppress the common-mode noise by 13 dB at the peak amplitude.

H. Simulation Analysis of Loss Distribution of Magnetic Components

To compare the power loss distribution of the magnetic components of the DAHB converter with that of the proposed converter, a three-dimensional FEM simulation was conducted. The maximum magnetic fluxes of the DAHB and the proposed converters were designed based on (31) and (32). The numbers of turns of L_1', L_2', L_3', and L_4' were set to 2, and those of L_1, L_2, L_3, and L_4 were set to 4. For a simple comparison, the same four layer magnetic structure as the one shown in Fig. 10 is used for the DAHB converter and the proposed converter. Serially connected windings L_1' and L_2' for the DAHB are constructed by parallelly connecting windings L_1 and L_2. In the same way, serially connected windings L_3' and L_4' are constructed by parallelly connecting windings L_3 and L_4. In this condition, the total winding volume, magnetic core volume, and maximum magnetic flux density are equal for the two converters. d_{PS} and d_{PP} are set to 2.0 and 8.0 mm, respectively. As additional input and output filters for the DAHB converter, a 1.2-μH inductor and a 0.6-μH inductor are assumed, respectively. The cross section of the windings in the filters is designed such that the dc resistances of the windings in the filters and those in the transformer of the converter are the same.

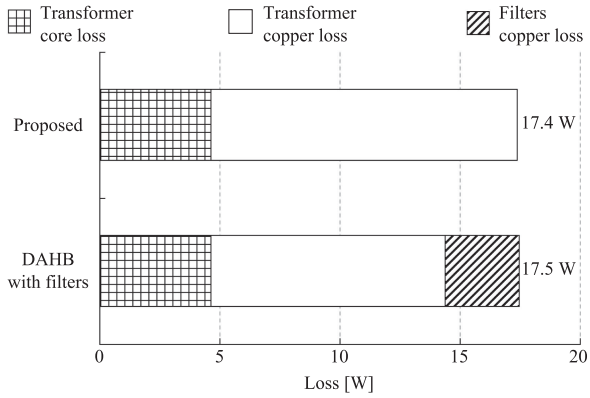

Fig. 15. Calculated distribution of the power losses of magnetic components at $V_{\mathrm{in}} = V_{\mathrm{out}} = 48$ V and $P_{\mathrm{out}} = 500$ W.

Fig. 15 shows the calculated distribution of the power losses of the magnetic components at $V_{\mathrm{in}} = V_{\mathrm{out}} = 48$ V and $P_{\mathrm{out}} = P_{\mathrm{out,DAHB}} = 500$ W. As we input currents to calculate the loss of the filters for the DAHB converter and the transformer windings in the proposed converter, an ac including a dc component was used. Because the current ripple in the filters is quite small, core loss of the filters cannot be seen in Fig. 15. Moreover, ac and dc conduction losses of the transformer winding in the proposed converter were calculated as a transformer copper loss.

The simulation result shows that the total power loss of the transformer for the proposed converter is almost the same as that of the transformer for the DAHB converter with additional filters. As the maximum magnetic flux and the magnetic core size are designed to be the same, core loss of the proposed converter attains the same value as that of the DAHB converter. Owing to the dc flowing in the windings, transformer copper loss of the proposed converter is higher than that of the DAHB converter. However, because the dc in the filters in the DAHB converter causes additional copper loss, the DAHB with the filters also has almost the same total copper loss.

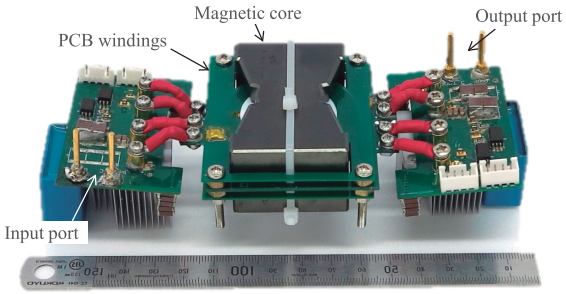

Fig. 16. Overview of the proposed converter prototype.

IV. Experimental System

To verify the operational principle of the proposed converter and compare it with the DAHB converter, prototypes of the proposed converter and DAHB converter were constructed, which are shown in Fig. 16. To design the leakage inductance precisely, windings are constructed from printed circuit boards (PCBs).

The circuit diagram of the experimental setup is shown in Fig. 17. The electric voltage sources and electric loads are connected to the input ports and output ports of both converters, respectively. The switching frequency is 200 kHz, and the input voltage $V_{\rm in}$ and output voltage $V_{\rm out}$ are set to 48 V. The winding ratios of the transformers are set to 1:1.

The designs of the maximum magnetic flux and the number of turns are the same as that of the simulation model used in the previous section. For fair comparison between the DAHB converter and the proposed converter, both the converters use an equal number of PCB windings (four turns; copper thickness: 175 μm). The DAHB converter uses two boards in parallel for L_1', L_2', L_3', and L_4'. The proposed converter uses one board for L_1, L_2, L_3, and L_4. In this condition, the total winding volume, magnetic core volume, and maximum magnetic flux density are equal for the two converters.

Table II summarizes the parameters of the electrical components in the DAHB converter and the proposed converter. To compare the current ripples under the same conditions, the same capacitance values are implemented in each part of the two converters, as summarized in Table II. The current ripple was measured using a spectrum analyzer (Keysight N9030 A). The number of points was set to 3000, and the measured frequency band was from 10 kHz to 30 MHz. The resolution bandwidth was set to 51 kHz and the video bandwidth was set to 150 kHz.

V. Experimental Results

Fig. 18 shows the operational waveforms of the DAHB converter and the proposed converter when the output power is 500 W. $v_{\rm L1}$, $v_{\rm L2}$, $v_{\rm P}$, and $v_{\rm S}$ show the transformer voltage of the proposed converter and the DAHB converter. Phase shifts in the proposed converter and the DAHB converter were similar when the output power was set to 500 W. $i_{\rm L1}$ and $i_{\rm P}$ show the transformer currents. The leakage inductance $L_{\rm eq}$ calculated from the transformer current is 1.21 μH, which corresponds to the value estimated using an LCR meter (1.14 μH). $i_{\rm diff}$ and $i_{\rm diff,DAHB}$ show the input currents of the proposed converter and the DAHB converter in the differential mode, respectively. The input current of the proposed converter was found to be smoother than that of the DAHB converter because of the zero-current-ripple operation.

TABLE II
Basic Parameters of the DAHB Converter and the Proposed Converter

Description	Property	
Switching frequency	$f_{\rm sw}$	200 kHz
Rated power	$P_{\rm out.max}$	500 W
Input and output DC voltage	$V_{\rm in},\ V_{\rm out}$	48 V, 48 V
Magnetic core	-	Ferrite PC9PQ60/42 (TDK)
Core gap	-	0.0 mm
Si MOSFET	$\rm S_1,\ S_2$ $\rm S_3,\ S_4$	IRFH7185TRPBF (Infineon)
DC capacitor	$C_1,\ C_2$ $C_3,\ C_4$	100 μF
DC capacitor	$C_{\rm in}, C_{\rm out}$	30 μF
DC capacitor	$C_{\rm in,tank}$, $C_{\rm out,tank}$	30 μF
Number of turns of primary side	$N_{\rm L1'}, N_{\rm L2'}$ $N_{\rm L1},\ N_{\rm L2}$	2, 2 4, 4
Number of turns of secondary side	$N_{\rm L3'}, N_{\rm L4'}$ $N_{\rm L3},\ N_{\rm L4}$	2, 2 4, 4
Equivalent leakage inductance	$L_{\rm eq,DAHB}$, $L_{\rm eq}$	0.29 μH, 1.14 μH
Self-inductance of primary side	L_1', L_2' $L_1,\ L_2$	80.6 μH, 80.6 μH 320.0 μH, 320.1 μH
Self-inductance of secondary side	L_3', L_4' $L_3,\ L_4$	80.6 μH, 80.6 μH 319.9 μH, 320.1 μH
Coupling coefficient	$k_{\rm PP}$	0.9981
Coupling coefficient	$k_{\rm PS}$	0.9990

Fig. 19 presents the spectrum analysis result for the differential-mode currents for an output power of 500 W. As a common-mode environment, including parasitic components, could not be constructed in the prototype, only differential-mode current was measured. The peak input current amplitude of the proposed converter is smaller than that of the DAHB converter (by 10 dB) for the frequency band over 1 MHz. As a whole, the proposed circuit can reduce noise as well as the simulation results; however, there are a few components where noise is deteriorated at certain frequency bands due to an imbalance between a magnetic element and a parasitic component. In the low-frequency band, 0.1–1 MHz, the noise of the proposed converter increases in the odd order and decreases in the even order. This means that the noise of the proposed converter is closer to a rectangular waveform than the noise of the DAHB converter. The rectangular wave current is generated owing to the imbalance of the circuit pattern and the impedance of the magnetic element. If the prototype is designed with attention to symmetry, the rectangular waveform will be a component that does not originally occur, as shown in the ideal waveforms (see Fig. 3). In the high-frequency band, 3–30 MHz, there are some portions where the noise of the proposed circuit is deteriorated owing to series resonance between an external circuit, a winding capacitance, or a filter capacitor and owing to the leakage inductances of a transformer.

Fig. 20 shows the measured and estimated efficiency curves of the proposed converter and the two types of DAHB converters. The larger DAHB converter is designed using a transformer core

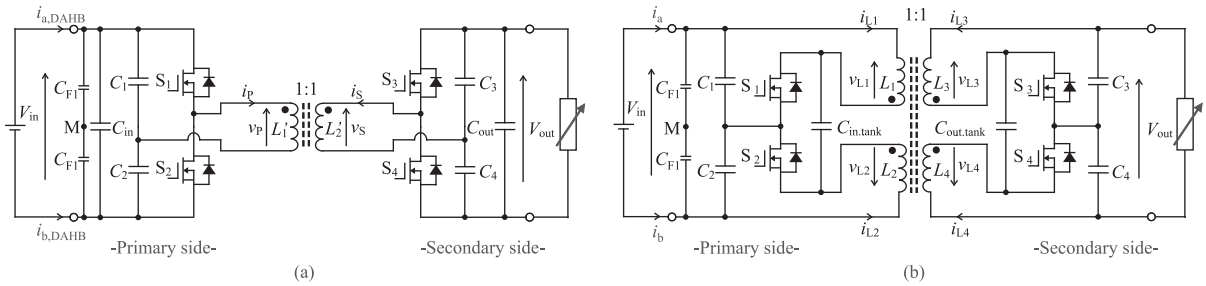

Fig. 17. Circuit diagram of the experimental setup of (a) the DAHB converter without filters and (b) the proposed converter with built-in filters.

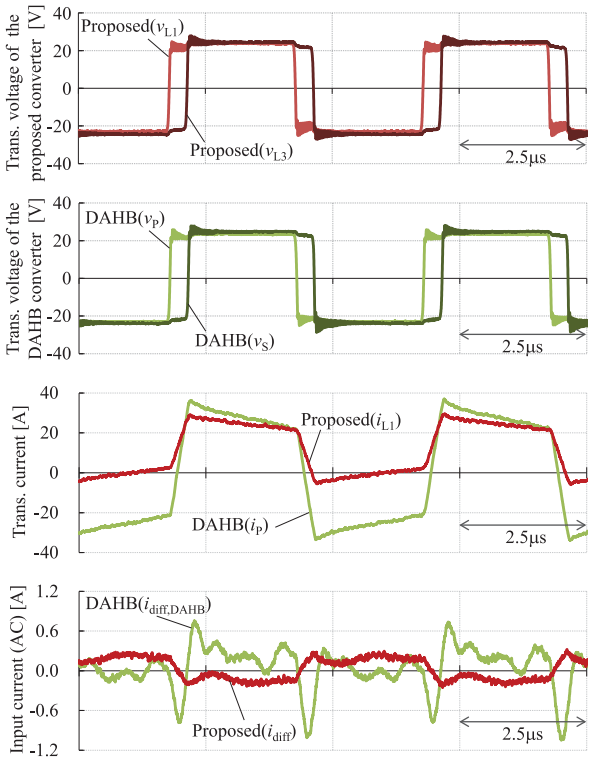

Fig. 18. Experimental waveforms of the DAHB converter and the proposed converter.

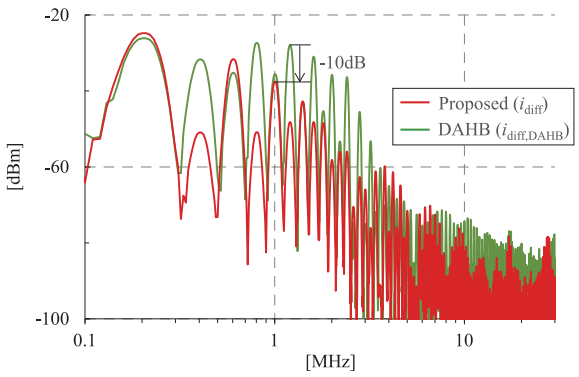

Fig. 19. Spectrum of the input current in the differential mode.

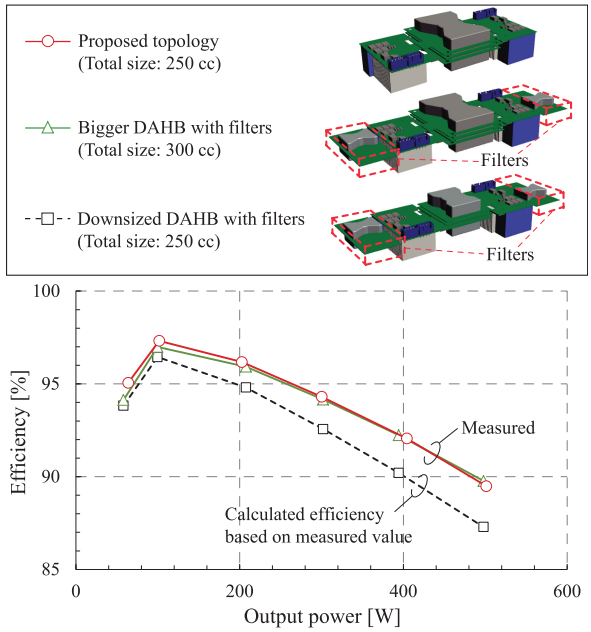

Fig. 20. Experimental results and estimated values of efficiency.

of the same size as that of the proposed prototype. Owing to the filter components, its overall size is larger than that of the proposed prototype by 50 cc. The assumed filters comprise two differential-mode filters (self-inductance: 1.2 and 0.6 μH) and two capacitors (50 and 50 μF). The total size of the downsized DAHB converter is reduced by narrowing the widths of the transformer windings and core window.

The circle and triangle marks indicate the measured efficiencies of the proposed converter and the DAHB converter, including the filter conduction loss, respectively. The efficiency curves of the proposed topology and the bigger DAHB with filters become almost the same in the entire power range. As has been shown in Fig. 15 that the losses of the magnetic components of the proposed converter are the same as those of DAHB with filters, the losses of the transistors in the proposed converter can be estimated to be the same as those in the DAHB. Therefore, the ZVS operation of the proposed converter is estimated to be performed at this operation point ($V_{\rm in} = V_{\rm out} = 48$ V) because the DAHB is operated in ZVS operation in this condition [15]–[17].

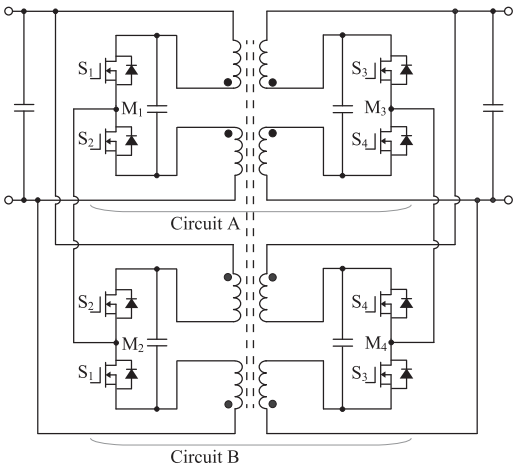

Fig. 21. Full-bridge-type dc–dc converter with built-in filters.

The square marks indicate the efficiencies of the downsized DAHB converter calculated based on its measured efficiencies. For the downsized effect of the transformer to reflect in the downsized DAHB converter, conduction loss caused by an additional ac resistance (65 mΩ) is added to the measured efficiencies of the DAHB converter.

At 500-W output power, the efficiency of the proposed prototype is higher than that of the downsized DAHB converter by 2% because the proposed converter integrates the filter components, and it can offer a wider width of windings compared with the downsized DAHB. Therefore, if the proposed converter is designed to be the same size as the DAHB converter, including the filter size, it will exhibit higher efficiency because the transformer size can be increased compared with the DAHB converter. In other words, compared with the DAHB converter, the proposed converter can improve power density or efficiency depending on the design.

VI. Discussion

In this section, a full-bridge type of the proposed converter is derived as an extension of the half-bridge-type dc–dc converter with built-in filters. Fig. 21 shows the full-bridge-type dc–dc converter with built-in filters. This topology has been derived from an analogy between the dual-active-full-bridge (DAFB) converter and the DAHB converter. Overall, the full-bridge-type converter is constructed by connecting the half-bridge-type converter in parallel, and using the control strategy similar to that of the half-bridge-type converter. A magnetic core is shared between Circuits A and B. The positions of the switch signals and the winding direction of the additionally connected circuit (Circuit B) are opposite to that of the original circuit (Circuit A). Since the mid-points in the half-bridge type of the proposed converter are connected to the same side of the circuits (M_1–M_2 and M_3–M_4), a full-bridge type of the proposed converter can eliminate series-connected capacitors. This relationship is the same as DAFB and can eliminate the series-connected capacitors in DAHB.

VII. Conclusion

This article presented a design theory for an isolated bidirectional dc–dc converter with built-in filters. The proposed converter helps eliminate the input and output filters that are used in a conventional DAHB converter. As the numbers of transistors, capacitors, and magnetic cores of the proposed converter are the same as those of the DAHB converter, the power density is directly impacted by the volume of the eliminated filter components at the input and output ports.

To clarify the advantages of the new circuit topology, the proposed converter and conventional DAHB converter are designed, constructed, and evaluated. The experimental results demonstrated that the proposed converter can suppress noise at the input port by 10 dB in the differential mode at a peak frequency over 1 MHz. If the two converters are designed for the same noise levels, including those of the input and output filters, the proposed converter can be designed with a wider width of the windings than the DAHB converter. Therefore, the proposed converter can provide higher efficiency compared with the DAHB converter because it reduces conduction losses owing to the additional width of the transformer windings.

In future work, a common-mode scheme with parasitic components will be constructed, and the common-mode noise will be compared between the conventional DAHB converter and the proposed converter to refine the design of the proposed converter considering differential- and common-mode noise.

References

[1] W. Zhang, D. Dong, I. Cvetkovic, F. C. Lee, and D. Boroyevich, "Lithium-based energy storage management for dc distributed renewable energy system," in *Proc. IEEE Energy Convers. Congr. Expo.*, 2011, pp. 3270–3277.

[2] K. Divya and J. Østergaard, "Battery energy storage technology for power systems overview," *Electr. Power Syst. Res.*, vol. 79, no. 4, pp. 511–520, 2009.

[3] *Energy Technology Perspectives 2017*, Int. Energy Agency, Paris, France, 2017.

[4] J. G. Kassakian, "Automotive electrical systems—The power electronics market of the future," in *Proc. 15th Annu. IEEE Appl. Power Electron. Conf. Expo.*, 2000, vol. 1, pp. 3–9.

[5] C.-M. Lai, Y.-C. Lin, and D. Lee, "Study and implementation of a two-phase interleaved bidirectional DC/DC converter for vehicle and dc-microgrid systems," *Energies*, vol. 8, no. 9, pp. 9969–9991, 2015.

[6] K. Hamada *et al.*, "Low loss high ruggedness PT-IGBT for 500 V variable voltage hybrid system," in *Proc. Int. Power Eng. Conf.*, 2005, vol. 2005, pp. 315–321.

[7] M. Pavlovsky, Y. Tsuruta, and A. Kawamura, "Bi-directional buck/boost DC-DC converter with ultra high efficiency based on improved SAZZ topology," in *Proc. IEEE Energy Convers. Congr. Expo.*, 2009, pp. 1783–1790.

[8] F. Krismer and J. W. Kolar, "Efficiency-optimized high-current dual active bridge converter for automotive applications," *IEEE Trans. Ind. Electron.*, vol. 59, no. 7, pp. 2745–2760, Jul. 2012.

[9] R. Hou, P. Magne, B. Bilgin, and A. Emadi, "A topological evaluation of isolated DC/DC converters for auxiliary power modules in electrified vehicle applications," in *Proc. IEEE Appl. Power Electron. Conf. Expos.*, 2015, pp. 1360–1366.

[10] S. Inoue, K. Itoh, M. Ishigaki, T. Sugiyama, and M. Sugai, "An isolated three-port DC-DC converter with high power density in 10 cm × 5 cm × 0.8 cm card size for flexible automotive systems," in *Proc. IEEE Energy Convers. Congr. Expo.*, 2016, pp. 1–8.

[11] Y. Yang, Z. Liu, F. C. Lee, and Q. Li, "Multi-phase coupled and integrated inductors for critical conduction mode totem-pole PFC converter," in *Proc. IEEE Appl. Power Electron. Conf. Expo.*, 2017, pp. 1804–1809.

[12] F. Musavi, W. Eberle, and W. G. Dunford, "A high-performance single-phase bridgeless interleaved PFC converter for plug-in hybrid electric vehicle battery chargers," *IEEE Trans. Ind. Appl.*, vol. 47, no. 4, pp. 1833–1843, Jul./Aug. 2011.
[13] D. S. Gautam, F. Musavi, M. Edington, W. Eberle, and W. G. Dunford, "An automotive onboard 3.3-kW battery charger for PHEV application," *IEEE Trans. Veh. Technol.*, vol. 61, no. 8, pp. 3466–3474, Oct. 2012.
[14] B. Bilgin, A. Emadi, and M. Krishnamurthy, "Design considerations for a universal input battery charger circuit for PHEV applications," in *Proc. IEEE Int. Symp. Ind. Electron.*, 2010, pp. 3407–3412.
[15] R. W. De Doncker, D. M. Divan, and M. H. Kheraluwala, "A three-phase soft-switched high-power-density DC/DC converter for high-power applications," *IEEE Trans. Ind. Appl.*, vol. 27, no. 1, pp. 63–73, Jan./Feb. 1991.
[16] S. Inoue and H. Akagi, "A bidirectional DC–DC converter for an energy storage system with galvanic isolation," *IEEE Trans. Power Electron.*, vol. 22, no. 6, pp. 2299–2306, Nov. 2007.
[17] F. Krismer and J. W. Kolar, "Accurate power loss model derivation of a high-current dual active bridge converter for an automotive application," *IEEE Trans. Ind. Electron.*, vol. 57, no. 3, pp. 881–891, Mar. 2010.
[18] *Vehicles, Boats and Internal Combustion Engines—Radio Disturbance Characteristics—Limits and Methods of Measurement*, 4th ed., Standard CISPR 25:2016, 2015.
[19] P.-L. Wong, P. Xu, P. Yang, and F. C. Lee, "Performance improvements of interleaving VRMs with coupling inductors," *IEEE Trans. Power Electron.*, vol. 16, no. 4, pp. 499–507, Jul. 2001.
[20] K. K. Hedel, "High-density avionic power supply," *IEEE Trans. Aerosp. Electron. Syst.*, vol. AES-16, no. 5, pp. 615–619, Sep. 1980.
[21] T. Qian and B. Lehman, "Dual interleaved active-clamp forward with automatic charge balance regulation for high input voltage application," *IEEE Trans. Power Electron.*, vol. 23, no. 1, pp. 38–44, Jan. 2008.
[22] L.-P. Wong, Y.-S. Lee, M. H. Chow, and D. K.-W. Cheng, "A four-phase forward converter using an integrated transformer," *IEEE Trans. Ind. Electron.*, vol. 55, no. 2, pp. 817–831, Feb. 2008.
[23] M. T. Zhang, M. M. Jovanovic, and F. C. Lee, "Analysis and evaluation of interleaving techniques in forward converters," *IEEE Trans. Power Electron.*, vol. 13, no. 4, pp. 690–698, Jul. 1998.
[24] B. Tamyurek and B. Kirimer, "An interleaved high-power flyback inverter for photovoltaic applications," *IEEE Trans. Power Electron.*, vol. 30, no. 6, pp. 3228–3241, Jun. 2015.
[25] J. C. Liu, N. Poon, B. M. Pong, and C. Tse, "Low output ripple dc-dc converter based on an overlapping dual asymmetric half-bridge topology," *IEEE Trans. Power Electron.*, vol. 22, no. 5, pp. 1956–1963, Sep. 2007.
[26] X. Wu, W. Lu, J. Zhang, and Z. Qian, "Extra wide input voltage range and high efficiency DC-DC converter using hybrid modulation," in *Proc. 41st Annu. Meeting IEEE Ind. Appl. Conf.*, 2006, vol. 2, pp. 588–594.
[27] X. Wang, F. Tian, and I. Batarseh, "High efficiency parallel post regulator for wide range input dc–dc converter," *IEEE Trans. Power Electron.*, vol. 23, no. 2, pp. 852–858, Mar. 2008.
[28] M. Hirakawa *et al.*, "High power DC/DC converter using extreme close-coupled inductors aimed for electric vehicles," in *Proc. Int. Power Electron. Conf.*, 2010, pp. 2941–2948.
[29] H. Kim, C. Yoon, and S. Choi, "An improved current-fed ZVS isolated boost converter for fuel cell applications," *IEEE Trans. Power Electron.*, vol. 25, no. 9, pp. 2357–2364, Sep. 2010.
[30] F. Deng and Z. Chen, "Control of improved full-bridge three-level DC/DC converter for wind turbines in a dc grid," *IEEE Trans. Power Electron.*, vol. 28, no. 1, pp. 314–324, Jan. 2013.
[31] L. F. Costa, S. A. Mussa, and I. Barbi, "Multilevel buck/boost-type DC–DC converter for high-power and high-voltage application," *IEEE Trans. Ind. Appl.*, vol. 50, no. 6, pp. 3931–3942, Nov./Dec. 2014.
[32] Z. Guo, K. Sun, and D. Sha, "Improved ZVS three-level DC–DC converter with reduced circulating loss," *IEEE Trans. Power Electron.*, vol. 31, no. 9, pp. 6394–6404, Sep. 2016.
[33] R.-S. Lai, K. Ngo, and J. Watson, "Steady-state analysis of the symmetrical push-pull power converter employing a matrix transformer," *IEEE Trans. Power Electron.*, vol. 7, no. 1, pp. 44–53, Jan. 1992.
[34] C.-S. Leu and J.-B. Hwang, "A built-in-input filter forward converter," in *Proc. 25th Annu. IEEE Power Electron. Spec. Conf*, 1994, vol. 2, pp. 917–921.
[35] P. Xu, M. Ye, P.-L. Wong, and F. C. Lee, "Design of 48 V voltage regulator modules with a novel integrated magnetics," *IEEE Trans. Power Electron.*, vol. 17, no. 6, pp. 990–998, Nov. 2002.
[36] S. Cuk, "A new zero-ripple switching DC-to-DC converter and integrated magnetics," *IEEE Trans. Magn.*, vol. 19, no. 2, pp. 57–75, Mar. 1983.
[37] S. Cuk and R. Middlebrook, "Advances in switched-mode power conversion. Part I," *IEEE Trans. Ind. Electron.*, vol. IE-30, no. 1, pp. 10–19, Feb. 1983.
[38] S. Cuk and R. Middlebrook, "Advances in switched-mode power conversion. Part II," *IEEE Trans. Ind. Electron.*, vol. IE-30, no. 1, pp. 19–29, Feb. 1983.
[39] S. Inoue, M. Ishigaki, A. Takahashi, and T. Sugiyama, "A novel filter built-in isolated bi-directional DC-DC converter with split windings," in *Proc. IEEE Appl. Power Electron. Conf. Expo.*, 2019, pp. 1567–1574.
[40] M. Shoyama, G. Li, and T. Ninomiya, "Balanced switching converter to reduce common-mode conducted noise," *IEEE Trans. Ind. Electron.*, vol. 50, no. 6, pp. 1095–1099, Dec. 2003.
[41] P. Kong, S. Wang, F. C. Lee, and Z. Wang, "Reducing common-mode noise in two-switch forward converter," *IEEE Trans. Power Electron.*, vol. 26, no. 5, pp. 1522–1533, May 2011.
[42] A. Takahashi, H. Tsukada, T. Kojima, Y. Hattori, T. Funaki, and O. Wada, "Analysis of common-mode noise generation mechanism in fm radio band caused by dc-dc converter," *R&D Rev. Toyota CRDL*, vol. 47, pp. 45–56, 2017.

Shuntaro Inoue (Student Member, IEEE) received the B.S. degree in mechanical engineering from Osaka University, Suita, Japan, in 2011, and the M.S. degree in precision engineering from the University of Tokyo, Tokyo, Japan, in 2013.

Since 2013, he has been with Toyota Central R&D Labs., Inc., Nagakute, Japan. His research interests include power electronics and mechatronics.

Mr. Inoue received the Japan Society of Mechanical Engineers Kansai-branch Best Presentation Award in 2011, the Institute of Electrical Engineers of Japan (IEEJ) Best Presentation Award in 2016, the IEEJ Encouragement Award in 2017, and the APEC 2019 Outstanding Presentation Award.

Masanori Ishigaki (Member, IEEE) received the B.S. degree in electrical engineering from Tokyo Metropolitan University, Tokyo, Japan, in 2005, and the M.S. degree in electrical and electronic engineering from the Tokyo Institute of Technology, Tokyo, in 2007.

Since 2007, he has been with Toyota Central R&D Labs, Inc., Nagakute, Japan. He was with the Electronics Research Department, Toyota Research Institute of North America, from 2014 to 2017. His research interests include electrical systems for vehicle electronics and power converter circuits.

Mr. Ishigaki was the recipient of the IPEC 2010 Second Prize Paper Award and the APEC 2012 and 2017 Outstanding Presentation Awards.

Atsuhiro Takahashi received B.E and M.E. degrees in engineering from Okayama University, Okayama, Japan, in 2007 and 2009, respectively.

Since April 2009, he has been with Toyota Central R&D Labs., Inc., Nagakute, Japan. His research interests include power electronics and its electromagnetic compatibility.

Mr. Takahashi is a member of the Institute of Electronics, Information and Communication Engineers.

Takahide Sugiyama (Member, IEEE) received the B.S. and M.S. degrees in electrical, electronics, and information engineering from the Nagoya Institute of Technology, Nagoya, Japan, in 1989 and 1991, respectively.

Since 1991, he has been with Toyota Central R&D Labs. Inc., Nagakute, Japan, where he is an R&D Team Manager for power supply systems for electrified vehicles. His research interests include power semiconductor devices.

Mr. Sugiyama is a member of the Institute of Electric Engineers of Japan and the Japan Society of Applied Physics.